Absolute evaluation of the optical transfer function of the high aperture infrared cryogenic objective

Joris Gorée, Edouard Huard de Verneuil, Jérôme Primot, Olivier Gravrand, Olivier Boulade, Sophie Derelle

Research Article | Vol. 32, No. 17 / 12 Aug 2024 / Optics Express 30609
Optics EXPRESS

Absolute evaluation of the optical transfer function of the high aperture infrared cryogenic objective

JORIS GORÉE,[1,*] EDOUARD HUARD DE VERNEUIL,[1] JÉRÔME PRIMOT,[1] OLIVIER GRAVRAND,[2] OLIVIER BOULADE,[3] AND SOPHIE DERELLE[1]

[1]*ONERA, Office National d'Étude et de Recherches Aérospatiales, Palaiseau, 91120, France*
[2]*CEA-LETI, Commissariat à l'Énergie Atomique et aux énergies Alternatives - Laboratoire d'Électronique et de Technologie de l'Information, 38054 Grenoble, France*
[3]*CEA-LETI, Commissariat à l'Énergie Atomique et aux énergies Alternatives - Institut de Recherche sur les lois Fondamentales de l'Univers, 91191 Saclay, France*
[*]*joris.goree@onera.fr*

Abstract: The field of infrared detectors is experiencing a strong movement towards smaller pixel pitches, and it is now common to see pitches close to the wavelength. This raises major problems in measuring their characteristics, especially their transfer function. The latter can be measured by optical pattern projection methods using a low F/# objective, such as the spot scan method. However, in order to obtain the quantitative transfer function measurement of detectors, the objective spatial response should be measured and deconvoluted precisely, since the size of the focused optical spot is close to the pixel pitch. Therefore, the purpose of this paper is to propose a protocol that performs an absolute measurement of a high-quality infrared objective. The main idea of the article is to link the measurement standard to a fundamental theory, the Huygens-Fresnel principle, using a particular wavefront sensor as a secondary measurement standard. This has various metrological advantages, that allow the uncertainties of the optical transfer function measurement to be controlled and evaluated. The protocol and the propagation of errors described in the article are both used to demonstrate the value of this approach.

1. Introduction

The development of the infrared FPAs' technology mirrors the evolution of the need for infrared imaging, especially when spectral and spatial resolution need to be higher at the request of scientific communities and optronic systems industry [1]. As a result, the quantum Focal Plane Array (FPA) tends to have a bigger format which is generally accompanied by a decrease in pixel size. For example, in the Midwave Infrared (MWIR) band, over the past 20 years, the pixel pitch has dropped from 30 µm through 15 µm [2,3], 12 µm [4] and 10 µm [5] to reach 7.5 or even 5 µm in recent publications [6,7]. Absolute spatial characterization (through Modulation Transfer Function (MTF) or Point Spread Function (PSF) measurements) are essential for both the detector designers (in order to precisely design optical systems) and the scientists (in order to operate and deconvolute scientific data) [8–11]. Some recent work [12] uses electronic beam scanning to restore the FPA's spatial response, but in this article, we will concentrate on optical measurement methods. Accurate FPA MTF and PSF optical measurements are harder to obtain when the pitch is close to the wavelength. This difficulty is linked to diffraction's limitation of the fineness of the optical patterns that can be projected onto the FPA. Typically, for a normalized FPA MTF between 0 and 1, an uncertainty on the FPA MTF amplitude less than 0.01 (1%) is a desirable (but yet hard to obtain) metrological target. To achieve this goal on FPA MTF, it is first necessary to know the Optical Transfer Function (OTF) of the test bench, at least to the same

#521266 https://doi.org/10.1364/OE.521266
Journal © 2024 Received 19 Feb 2024; revised 19 Apr 2024; accepted 19 Apr 2024; published 8 Aug 2024

Optics EXPRESS

level of precision, and it is on this latter point that this article focuses. Indeed, it is challenging to link a fundamental value with such MTF measurements. The following are the most common techniques and their associated metrological strategies.

Interferential and speckle techniques: for example, the FPA MTF can be estimated using the laser speckle-based approach [13]. This method does not require moving parts nor requires high-quality imaging optics. It is based on a diffuser placed upstream of a scattering aperture [14,15]. It is also linked to a fundamental principle, speckle interference theory, but it has its own inherent limitations regarding the power spectral density estimation, which is needed to extract MTF data [16]. Recent research found a way to accurately estimate the MTF of FPAs when the Fresnel approximation is violated [17].

Pattern metallization techniques: one method [18] consists of uniformly illuminating the back of the FPA, gold-coated with 4 μm square holes in precise locations. No scanning or imaging with high-quality optics are required since this implies a spatial uniformity of illumination, allowing the reconstruction of the PSF of the pixel while assuming that the pixels are identical. However, the smaller the pixel pitch, the finer the metallization pattern is required (sub-lambda size), raising questions about possible unwanted optical diffraction effects within the pattern, that should be taken into account for absolute measurements.

Optical projection techniques: the projection of an object pattern (slanted edge, slit, hole for spot scan. . .) using a high-quality infrared objective is a very common category of FPA MTFs measurement techniques [19–22]. Nonetheless, in order to achieve absolute MTF measurement of the FPA, the characterization should be followed by an absolute deconvolution of the measurement system OTF. This deconvolution is even more crucial when pixel size gets closer to the wavelength, because the size of the impulse function of the optics used (the Airy spot for perfect diffraction limit optics) is very close to the pixel pitch [23].

In this article, we focus on the latest category and demonstrate a new method for obtaining absolute objective OTF characterization. The proposed protocol uses the application example of the characterization of a mid-infrared high-aperture spot scan objective. The choice of this example was driven by the simplicity of the spot scan principle, which makes the absolute measurement of OTF, among the other possible noise and bias sources (detector noise, scanning issues), a major contributor to the metrological quality of the spot scan result, particularly for pixels of size close to the wavelength. However, the protocol could easily be adapted for slits and slanted edge methods, as well as any other application where an absolute optical characterization is required. The considered infrared objective has an aperture of F/1 ($N_{aperture} = 1$), with a 25mm pupil diameter. Nonetheless, in our spot scan configuration, in order to reduce the infrared thermal background and to precisely work on the optical axis of the objective, the latter is used in a finite conjugation: a 15μm object hole is placed at 150mm in front of the objective, so that, at this conjugation, the geometrical image of the 15μm object hole is smaller than the diffraction Airy disk. The spot is imaged 30mm behind the objective, leading to image aperture angle of $\theta_{aperture} = 22.6°$ (equivalent to $N_{aperture} \cong 1.2$). The choice of this high aperture is driven by the pixel size. Typically, we need the focal spot to be smaller than the pixel size, so that $2\lambda \times N_{aperture} <$ pixel size, which means $N_{aperture} < \frac{pixel\ size}{2\lambda}$, i.e., with typically a pixel size of 10μm and at $\lambda = 4$μm, $N_{aperture} < 1.25$, which is the case here.

The metrology protocol, which relies on the Huygens-Fresnel principle through the calibration of our working measurement standard (the mid-infrared objective), will be described in section 2 at a wavelength at 3.75μm, and error propagation through measurement will be analyzed in section 3.

2. OTF measurement through the Huygens-Fresnel principle

The strategy adopted to achieve an absolute measurement of the objective is illustrated in Fig. 1. The idea is to compare in-situ the primary standard wavefront to the working standard wavefront

Optics EXPRESS

using a wavefront analyzer, to eventually compute the OTF of the working standard. This section will describe the different parts of the protocol, from the primary standard to the measurement of the working standard wavefront and OTF.

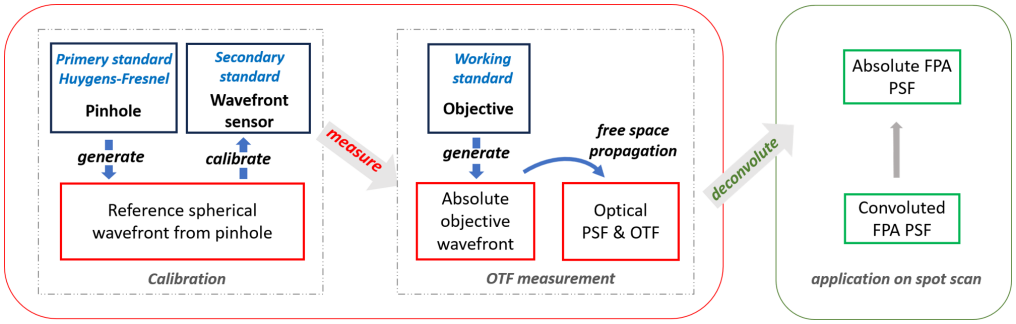

Fig. 1. Overall description of the metrological strategy (on the left), and example of absolute spot scan application (on the right). Red quantities are described and computed in the article, while green quantities are left to the end user.

2.1. Primary and secondary standards

Since an absolute characterization of the objective OTF is required, the quantitative measurement must be linked to a fundamental optical principle. The Huygens-Fresnel principle was considered a good candidate: firstly, its theory and experimental implementation are straightforward and well described in the scientific literature [24,25] and, secondly, the spherical wave diffracted by an ideal point source has the same wavefront shape as the ideal optical spot focused on the FPA. Consequently, the starting point of our metrology is simply to use a circular diffractive hole which will be our primary standard. The size of the hole is chosen in conformity with the wavelength in order to achieve a diffraction point source.

Reference [26] demonstrate the validity of using a wavelength-sized pinhole under converging illumination to generate a spherical reference. According to [27] which uses the same principle to calibrate a Shack–Hartmann sensor in the visible range, a diffractive hole can be used as a spherical reference if its diameter D_{hole} is nearly equal to 0.5 * lambda / N.A., where N.A. is the numerical aperture over which the spherical reference should be accessible. In our case, the numerical aperture we need to address is linked to the spot scan configuration: with the air refraction index approximated to 1, this numerical aperture is then equal to $\sin(\theta_{aperture}) = \sin(22.6\,\text{deg}) \cong 0.38$, which should be compared to $\frac{\lambda}{2D_{hole}} \cong 0.38$ at $\lambda = 3.75\mu\text{m}$ and $D_{hole} = 5\mu\text{m}$. In the infrared range, the size of the hole should be a trade-off between diffraction criterion and noise-to-signal ratio criterion. The size of $D_{hole} = 5\mu\text{m}$, which is the upper limit in respect to the spherical criterion, was therefore chosen. Reference [27] and also a paper on the Rayleigh-Sommerfeld Fraunhofer diffraction, concerning in the Fraunhofer conditions and the impact of the inclination factor approximation [28], remind us here that there is a point to watch out with other choices of diffractive holes (depending on the application), especially if we are considering larger apertures, or using holes of non-negligible size.

Besides, the distance $Z_{det} = 9mm$ between the reference hole and the wavefront sensor has been calculated to ensure agreement between the usable aperture of the primary standard and that of the working standard, in relation to the size of the analyzer's detector (320×256 array with 30µm pixel pitch). In those conditions, we can compute that Fresnel number $N_{Fresnel}$ is sufficiently small, so that we are in the Fraunhofer regime for λ between 3 and 5µm, and at the distance Z_{det} the wavefront can be supposed perfectly spherical. For example at $\lambda = 3\mu\text{m}$, we

Optics EXPRESS

have:

$$N_{Fresnel} = \frac{D_{hole}^2}{Z_{det}\,\lambda} \approxeq 0.001 \lll 1 \tag{1}$$

The objective and the diffractive hole are illuminated by a collimated infrared beam from a blackbody. The latter is a cavity-type blackbody at 1200 °C with a 4mm pinhole placed at the focal plane object of the collimator, such as illustrated in Fig. 2. The collimated beam then enters the cryogenic bench and is focused by the objective, which acts as a condenser, so that the reference pinhole is properly illuminated. The general set-up principle is similar to Refs. [26,27], with the strong constraint of the infrared cryogenic environment.

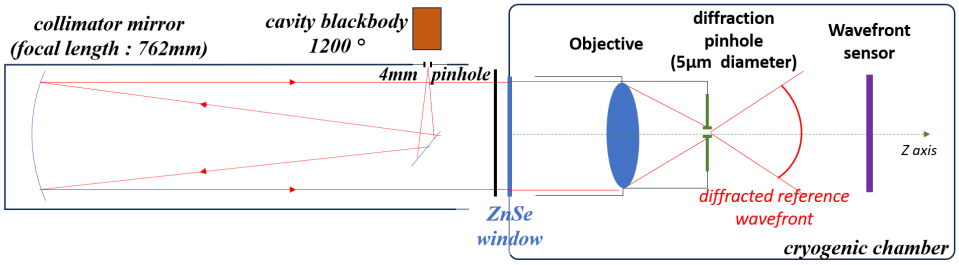

Fig. 2. General set-up: a cavity-type black-body is placed in the focal plane of a 762mm collimator, and the collimated beam enters the cryogenic chamber by a ZnSe window. Inside the chamber, the cryogenic objective is used as a condenser for the calibration step.

In order to compare this reference wave with the working objective wave, a wavefront analyzer is used and acts as a secondary measurement standard. The hole, illuminated by the black body through the working standard objective, is placed upstream of the analyzer within the same cryogenic bench (Fig. 3). The choice to use the working standard objective as a projecting system for calibration is made to minimize the set-up changes between the calibration step and the final measurement of the working standard wavefront, so that calibration and final measurement steps take place in the exact same cryogenic set-up conditions.

In the following discussion, $W_{ref}(x, y)$ will represent, in the analyzer plane, the spherical reference wavefront coming from the diffractive hole and $W_{obj}(x, y)$ will represent, in the analyzer plane, the wavefront coming from the infrared objective. Each of these quantities is a local distance of the corresponding wavefront referenced from the analyzer plane (Ox, Oy).

The wavefront analyzer used in this calibration is the (QWLSI) placed in the plane (O, x, y), where O is the center of the grating. The QWLSI is based on a specific 2D grating called Modified Hartmann Mask (MHM) [29,30], and contrary to the Shack-Hartmann experiment in Ref. [26,27], no coupling optics is needed between the diffraction pinhole and the sensor since the QWLSI can work with converging or diverging beams as well as collimated ones [31]. It diffracts four tilted replicas of the incoming beam that constitute the first four orders of the grating in the transverse directions (x, y and $-x, -y$) of the analyzer plane. The shape of the interferogram obtained by overlapping these replicas depends on the gradients of the incoming wavefront (that is to say $W_{ref}(x, y)$ during the calibration step) in the orthogonal directions (Ox, Oy) of the coupled grating orders and their diagonals [32]. Extraction and integration over these gradients is then conducted through a specific algorithm to retrieve the entire incoming wavefront [33]. For the purpose of the experiment, the QWLSI is placed upstream at 4 mm from the 30 µm pitch 320 by 256 pixels HgCdTe FPA, and the grating period is equal to 240 µm, so that the captured interferogram is properly sampled on the infrared FPA. The reference interferogram is illustrated in Fig. 4(c).

Optics EXPRESS

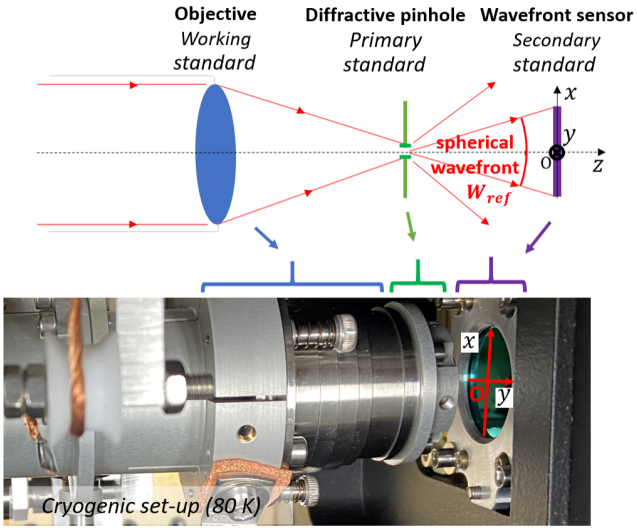

Fig. 3. Calibration principle of the wavefront analyzer using diffraction pinhole. $W_{ref}(x, y)$ is the wavefront coming from the pinhole, in the analyser plane, and (x, y) are the orders' axis of the (QWLSI) analyzer.

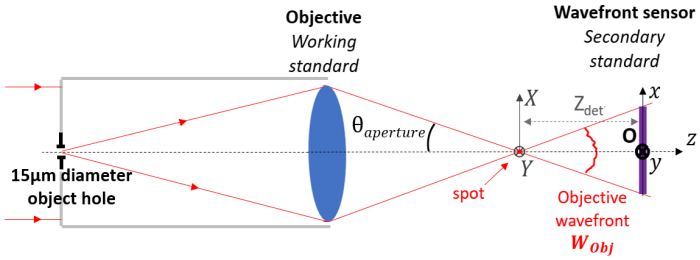

(a) Measurement of objective wavefront $W_{obj}(x, y)$

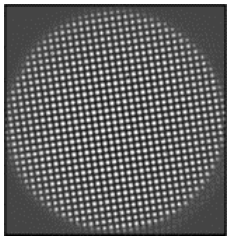

(b) Objective wavefront interferogram

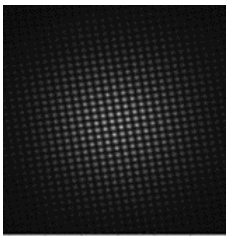

(c) Reference wavefront interferogram

Fig. 4. Measurement of the objective wavefront $W_{obj}(x, y)$(a), and associated interferogram (b) which is then confronted to calibration interferogram (c) captured in the previous configuration of Fig. 3. Interferograms are in the (x, y) plane, whereas the focused spot is in the (X, Y) plane. The distance between those planes is $Z_{det} = 9$ mm so that the objective pupil is complete and sufficiently sampled.

Optics EXPRESS

2.2. Working measurement standard analysis

Once the analyzer has been calibrated with the primary measurement standard described in section 2.1, the reference hole is removed and the wavefront $W_{obj}(x, y)$ generated by the spot scan objective is measured, as shown in Fig. 4.

As previously said, the typical distance between the focal plane of the objective and the analyzer is 9 mm, so that the projected pupil of the objective covers as much of the FPA surface as possible, while still being fully visible on the acquired image. Since wavefront analysis is spectral, filters are placed upstream of the objective in order to monitor the black body spectrum. In this article, we present the results obtained with a 500 nm Full Width at Half Maximum (FWHM) centered at 3.75 µm.

Once the interferograms have been acquired, a reconstruction algorithm [33] is applied to determine the absolute deviation $W_{abs}(x, y)$ of the objective wavefront from the perfect spherical reference wave (called the normal deviation from the sphere) [Fig. 5] :

$$W_{abs}(x, y) = W_{obj}(x, y) - W_{ref}(x, y) \tag{2}$$

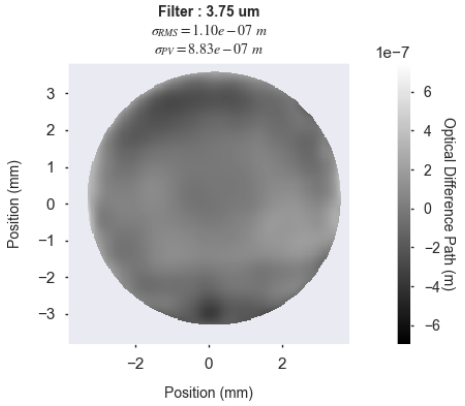

Fig. 5. The wavefront reconstruction $W_{abs}(x, y)$ represents the difference between the wavefront coming from the objective and the one coming from the reference wavefront.

Firstly, the Peak-to-Valley (PV) and Root Mean Squared (RMS) standard deviations are $\lambda/5$ and $\lambda/35$ at $\lambda = 3.75$ µm, which means the objective presents high optical quality. For the spot scan application, these results establish that the wavefront is not too aberrant for the deconvolution step to work properly. In addition, the decomposition of the wavefront based on the Zernike polynomials makes it possible to analyze the aberration types generated by the objective, as illustrated in Fig. 6. For the sake of clarity, the tilt and defocus have been removed as they are related to the optical bench layout.

The astigmatism and the coma aberrations are predominant. Their presence might be due to the optical system's eccentricity which can be triggered by thermal effects during thermal cooling cycles, or by mechanical assembly default. However, the magnitude of Zernike coefficients suggests that the eccentricity is very small.

2.3. From the wavefront to the OTF

The absolute wavefront $W_{abs}(x, y)$ was measured in the wavefront analyzer detector plane. For the spot scan application, we need to perform deconvolution in the focal plane of the objective. In order to get the PSF and associated OTF in this focal plane, we compute free space propagation using classical Fourier wave optics theory. The final OTF result is presented on Fig. 7.

Optics EXPRESS

Z_0^0 / Z_0	Piston	0.00e+00
Z_1^{-1} / Z_1	Tilt 90°	0.00e+00
Z_1^1 / Z_2	Tilt 0°	0.00e+00
Z_2^{-2} / Z_3	Astigmatism 45°	-5.06e-10
Z_2^0 / Z_4	Defocus	0.00e+00
Z_2^2 / Z_5	Astigmatism 0°	7.32e-08
Z_3^{-3} / Z_6	Trefoil 30°	2.31e-08
Z_3^{-1} / Z_7	Coma 90°	-6.01e-08
Z_3^1 / Z_8	Coma 0°	-3.05e-08
Z_3^3 / Z_9	Trefoil 0°	3.18e-09
Z_4^{-4} / Z_{10}	Tetrafoil 22,5°	9.22e-09
Z_4^{-2} / Z_{11}	Astigmatism 2^{nd} order 0°	3.30e-09
Z_4^0 / Z_{12}	Spherical Aberration	2.33e-08
Z_4^2 / Z_{13}	Astigmatism 2^{nd} order 0°	-6.77e-09
Z_4^4 / Z_{14}	Tetrafoil 0°	1.25e-08
Z_5^{-5} / Z_{15}	Hexafoil 18°	-3.26e-09
Z_5^{-3} / Z_{16}	Trefoil 2^{nd} order 30°	1.06e-08
Z_5^{-1} / Z_{17}	Coma 2^{nd} order 90°	-2.74e-08
Z_5^1 / Z_{18}	Coma 2^{nd} order 0°	-1.79e-08
Z_5^3 / Z_{19}	Trefoil 2^{nd} order 0°	1.11e-08
Z_5^5 / Z_{20}	Hexafoil 0°	4.33e-09

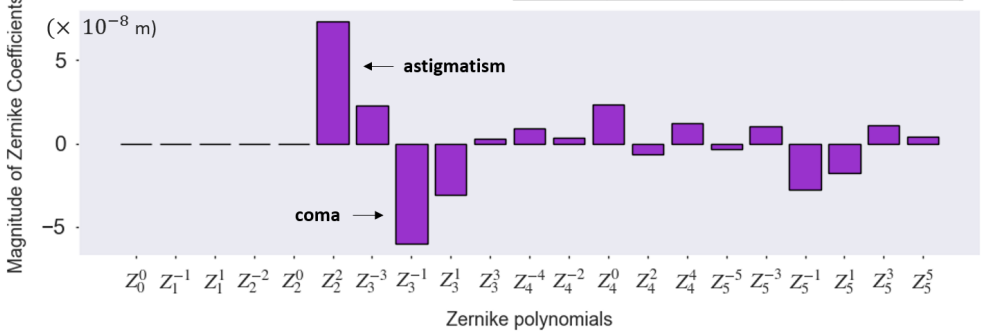

Fig. 6. Fitting with the Zernike polynomials and Zernike Coefficients (Zernike polynomial convention from Ref. [34]).

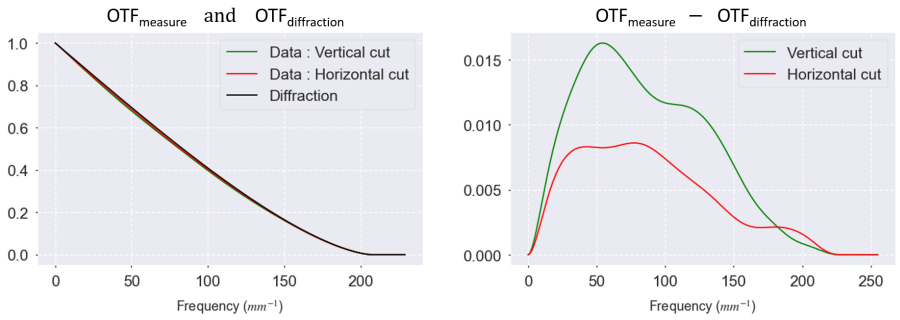

Fig. 7. OTF cross-sectional views. On the left are the diffraction theorical curve, and experimental OTF in x and y directions. On the right is the difference between experimental and diffraction curves.

Linked with the small measured wavefront aberrations, we can observe a minor degradation of the OTF values from diffraction limit, especially in the mid-frequencies (low and high frequencies are very close to diffraction), which is typical of optics design. The overall degradation is low (less than 0.02) but is still comparable to the MTF accuracy required for FPA MTF measurements (0.01) and this shows the importance of the OTF deconvolution for detector spatial characterization. The key here is that the objective can be used as a working measurement standard whose spatial response is known quantitatively.

3. Estimates of measurement uncertainties and biases

The purpose of this section is to propagate the error on the final OTF result. Beforehand, we need to estimate the noise standard deviation σ_W of the reconstructed objective wavefront $W_{abs}(x, y)$. To do so, a simple measurement of the standard deviation in a small area of the pupil wavefront is not enough, as it is impossible to know whether we are analyzing the standard deviation of the Optical Path Difference (OPD) (which is related to the term σ_{RMS}) or the standard deviation σ_W

Optics EXPRESS

of the measurement noise itself. Instead, a tool inherent to QWLSI, that provides direct feedback on the quality of the analysis, is used.

3.1. Measurement noise estimates: PDCM

As seen in the previous section, the interferogram first provides information on the wavefront gradients. Using the derivatives over x and y, the errors in the measurement can be traced through what is known as the (PDCM). It is expressed as follows [35]:

$$PCDM(x,y) = \partial_x \left[\partial_y W(x,y)\right] - \partial_y \left[\partial_x W(x,y)\right] \tag{3}$$

With $W_{abs}(x,y)$, the OPD at the point (x,y), and the notation ∂_x is the partial derivation : $\frac{\partial}{\partial x}$.
In the case of an error-free wave surface, we would have:

$$\forall (x,y) : PCDM(x,y) = 0. \tag{4}$$

However, the PDCM will not equal zero if at least one of these 3 errors occurs [35]: A first error e_b due to measurement noises (FPA, optics...), a second error e_s due to the presence of phase jump or dislocations, and a third error e_e due to the frequency undersampling of the measurement (error evolving spatially too fast compared to the frequency sampling).

In our case (measure of a high-quality objective), no wavefront dislocations are measured, and the chosen sampling is sufficiently small compared to the measured error. Consequently, we can hypothesize that $e_s, e_e << e_b$, and thus we can approximate:

$$\forall (x,y) : PCDM(x,y) \cong e_b(x,y). \tag{5}$$

Thus, the spatial standard deviation σ_{PDCM} of the PCDM is directly equal to that of the spatial noise $e_b(x,y)$. In practice, the PDCM is computed numerically via Eq. (6), resulting in confidence map as illustrated in Fig. 8, and then σ_{PDCM} is then calculated.

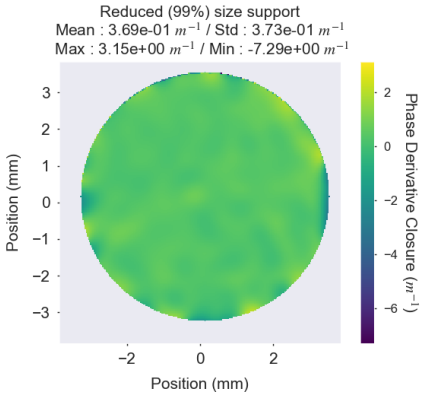

Fig. 8. Phase Derivatives Closure Map. Computation is made over 99% of the surface of the pupil, in order to avoid edge issues.

In order to avoid Gibbs effects on the noise estimation, the 1% edge values are not taken into account for the computation of the standard deviation σ_{PDCM} of the PDCM, and we obtained $\sigma_{PDCM} = 3.73\times10^{-1}$ m^{-1}.

According to Southwell [36], Freischald and Koliopoulos [37], when the wavefront is estimated using the least-squares method, the standard deviation σ_W of the noise in the reconstructed wavefront is proportional to the standard deviation of the noise $e_b(x,y)$:

$$\sigma_W = R \times \sigma_{PDCM}. \tag{6}$$

where R is the proportional factor which could be retrieved from simulation.

Optics EXPRESS

3.2. Establishment of the ratio R

In order to determine the ratio R, a noisy sample simulation under the same measurement conditions is used to generate interferograms of different wavefront noise levels. From each of these interferograms, a reconstructed image and a PDCM are also generated and analyzed for standard deviation evaluation. The ratio R is obtained by looking at the evolution of the standard deviation in the PDCM in relation to the standard deviation of the measurement noise implemented into the input wavefront, as illustrated in Fig. 9.

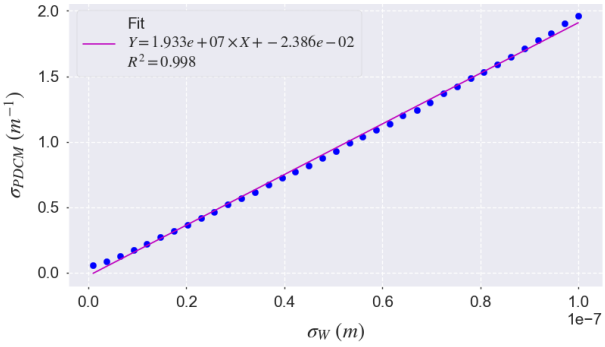

Fig. 9. Ratio evaluation through simulation.

Applying the curve fitting to the data enables us to obtain the ratio R which is 2×10^{-7} m^{-2}. This value will lead to the standard deviation value of the measurement noise which is 1.87×10^{-8} m. For a filter used at 3.75 µm, the standard deviation of the measurement noise σ_W is estimated at $\approx \lambda/200$ which is nearly ten times less than the standard deviation of the OPD.

3.3. Relation between the measurement noise and the OTF error

The link between σ_W and σ_{OTF} has been here established in the case of a white phase noise. The demonstration and its hypotheses, presented in the appendix of the article, leads to the following formula: For $(f_x,f_y) \neq (0,0)$:

$$\sigma_{OTF}(f_x,f_y) \cong \left(\frac{2\pi\sigma_W}{\lambda}\right)^2 OTF(f_x,f_y) \tag{7}$$

In the particular case of our experiment, with $\sigma_W \approx \lambda/200$, the quantity $\left(\frac{2\pi}{\lambda}\right)^2\sigma_W^2$ equals 0.001, which should be compared to the required error of 0.01 for MTF measurements. Therefore, when applied to spot scan measurements, the optical deconvolution error will be negligible compared to the required MTF error, guaranteeing metrological control of these measurements.

4. Conclusion

In this paper, an absolute measurement using the Huygens-Fresnel principle is used for the characterization of a high aperture infrared cryogenic objective. Thanks to the QWLSI wavefront analyzer used as the secondary standard measurement, the quality of the working standard has been established. The inherent features of the QWLSI have made it possible to establish the standard deviation of the wavefront measurement noise using the PDCM approach, and then the link between wavefront noise and OTF was derived. Among the other possible metrological uses of this method, those results are of interest for absolute FPA MTF characterization, and will soon be applied to the study of small-pixel FPAs.

Optics EXPRESS

A. Appendix

Notations and purpose

We consider the transverse pupil coordinates (x, y) in the wavefront analyzer plane, and the coordinates (X, Y) in the focalized spot image plane. We define $\phi_{obj}(x, y) = \frac{2\pi}{\lambda} W(x, y)$ as the difference between the real phase wavefront of the lens and the spherical reference wavefront. The associated complex amplitude will be denoted A_{obj} so that:

$$A_{obj}(x, y) = S_{pupil}(x, y) \times \exp(i\phi_{obj}(x, y)) \tag{8}$$

where S_{pupil} is the image pupil surface of the objective.

We then define A_{mes}, ϕ_{mes} as the complex amplitude and phase associated with the noisy measured OPD, measured on the pupil surface $S_{pupil}(x, y)$. The phase measurement noise will be denoted ε_ϕ, so that:

$$\phi_{mes}(x, y) = \phi_{obj}(x, y) + \varepsilon_\phi(x, y) \tag{9}$$

In this appendix, we demonstrate the link between the OTF error and the initial phase measurement error. We will first see the equations in the general case (small error $\varepsilon_\phi(x, y)$ but the arbitrary phase of objective ϕ_{obj} is not necessarily small), and then we will see the particular case of a high-quality objective (small phase error $\varepsilon_\phi(x, y)$ and small phase difference ϕ_{obj} thanks to low optical aberrations).

General case

With the described notations, we can compute:

$$\begin{aligned} A_{mes}(x, y) &= S_{pupil}(x, y) \times \exp(i\phi_{mes}(x, y)) \\ &= S_{pupil}(x, y) \times \exp(i\phi_{obj}(x, y)) \times \exp(i\varepsilon_\phi(x, y)) \\ &= A_{obj}(x, y) \times \exp(i\varepsilon_\phi(x, y)) \end{aligned} \tag{10}$$

On the hypothesis of a small phase error comparing to the measured phase value (for the record we have here a phase error of $\sigma_W \approx \lambda/200$ for a typical measured phase value of $\lambda/5$ PV and $\lambda/35$ RMS), so we can write $\varepsilon_\phi << \phi_{obj}$, we can then make the following Taylor series first order approximation:

$$\begin{aligned} A_{mes}(x, y) &\cong A_{obj}(x, y) \times (1 + i\varepsilon_\phi(x, y)) \\ &\cong A_{obj}(x, y) + iA_{obj}(x, y) \times \varepsilon_\phi(x, y) \end{aligned} \tag{11}$$

The noisy measured optical transfer function OTF_{mes} can be written as an autocorrelation function of A_{mes}:

$$OTF_{mes}(f_x, f_y) = \langle A_{mes} \rangle = A_{mes} * \overline{A_{mes}} \tag{12}$$

where $\langle\ \rangle$ is the spatial autocorrelation, $*$ is the spatial convolution product and $\overline{A}$ is the complex conjugate of A. The coordinates $(f_x, f_y) = (\frac{X}{\lambda d}, \frac{Y}{\lambda d})$ are the dual coordinates of (X, Y) in the Fourier image plane, with $d = 9$ mm the distance between the (x, y) image pupil plane and the (X, Y) focalized spot plane. For ease of reading, coordinates are omitted in the following formula. We

Optics EXPRESS

have then:

$$\begin{aligned} OTF_{mes} &= \left(A_{obj} + iA_{obj} \times \varepsilon_\phi\right) * \left(\overline{A_{obj} + iA_{obj} \times \varepsilon_\phi}\right) \\ &= \left(A_{obj} + iA_{obj} \times \varepsilon_\phi\right) * \left(\overline{A_{obj}} - i\ \overline{A_{obj}} \times \varepsilon_\phi\right) \\ &= \langle A_{obj} \rangle + \langle \varepsilon_\phi \times A_{obj} \rangle - i\, A_{obj} * \left(\overline{A_{obj}} \times \varepsilon_\phi\right) + i\, \overline{A_{obj}} * \left(A_{obj} \times \varepsilon_\phi\right) \\ &= \langle A_{obj} \rangle + \langle \varepsilon_\phi \times A_{obj} \rangle \\ &= OTF + \langle \varepsilon_\phi \times A_{obj} \rangle \end{aligned} \tag{13}$$

We can then identify the right term to be the error realization on the OTF : $\delta_{OTF}(f_x,f_y) = \langle \varepsilon_\phi \times A_{obj} \rangle (f_x,f_y)$. It is worth noting here that the OTF error results from the autocorrelation of a quantity related to the aberrant phase of the objective and its noise. In the case of weakly spatially correlated noise (which in practice is the case of the analyzer detector noise), we will observe an error peak around zero frequency, linked to the noise autocorrelation.

Particular case of a high-quality objective

The term $\varepsilon_\phi \times A_{obj}$ can be further analysed, if we make a hypothesis of a high-quality objective, we can apply a second Taylor series first order approximation: $\exp(i\phi_{obj}) \cong (1 + i\phi_{obj})$. This approximation means here we do consider that very low amplitude aberration has a negligible impact on the measurement. Typically for the worst case scenario here: $\lambda/5$ error (which is the peak-to-valley value), the second order in Taylor serie is here $\frac{(\lambda/5)^2}{2} = \lambda/50$.

We can then compute the product $\varepsilon_\phi \times A_{obj}$:

$$\begin{aligned} \varepsilon_\phi \times A_{obj} &= \varepsilon_\phi \times S_{pupil} \times (1 + i\phi_{obj}) \\ &= S_{pupil} \times \varepsilon_\phi + iS_{pupil} \times \varepsilon_\phi \times \phi_{obj}. \end{aligned} \tag{14}$$

The wavefront estimation error $\varepsilon_\phi(x,y)$ and the wavefront $\phi_{obj}(x,y)$ are supposed to be spatially and temporally uncorrelated. So the autocorrelation of $\varepsilon_\phi \times \phi_{obj}$ will be statistically close to zero. Thus we have:

$$\delta_{OTF} = \langle S_{pupil} \times \varepsilon_\phi \rangle \tag{15}$$

We can assume uncorrelated (white) phase measurement noise. This hypothesis is valid only for a sufficiently sampled wavefront, i.e. with low-amplitude and slowly variable aberrations (as compared to the size of the pixels of the analyser's detector), which is the case here since $\sigma_{\mathrm{RMS}} = \lambda/35$ (so $\phi_{obj} << 2\pi$) and low-order aberrations (coma, astigmatism of first and second orders) are predominant. The phase noise $\varepsilon_\phi(x,y)$ can be expressed by the following expression:

$$\varepsilon_\phi(x,y) = \frac{2\pi}{\lambda}\sigma_W\ d_{white}(x,y) \tag{16}$$

where σ_W is the standard deviation of the wavefront measurement noise, computed in section 3.2 (σ_W is a scalar), d_{white} a white noise distribution. Then we have:

$$\begin{aligned} \delta_{OTF} &= \langle \varepsilon_\phi \times A_{obj} \rangle (f_x,f_y) \\ &= \frac{2\pi}{\lambda}\sigma_W\ \langle\ d_{white} \times S_{pupil} \rangle \end{aligned} \tag{17}$$

For $(f_x,f_y) \neq (0,0)$, we finally have the relation:

$$\sigma_{OTF}(f_x,f_y) \cong \left(\frac{2\pi\sigma_W}{\lambda}\right)^2\ OTF(f_x,f_y) \tag{18}$$

Optics EXPRESS

Funding. Agence Nationale de la Recherche (ANR-11-LBX-001); Direction Générale de l'Armement.

Acknowledgements. This work is supported by the LabEx FOCUS gathering nine major laboratories that bring their expertise in the detection field to contribute to the development of better detectors for astronomy and Earth observation. We also thank Daniel Soler and Eric Tournayre for fruitful discussions.

Disclosures. The authors declare no potential conflict of interest related to this paper.

Data availability. Data underlying the results presented in this paper are not publicly available at this time but may be obtained from the authors upon reasonable request.

References

1. G. C. Holst and R. G. Driggers, "Small detectors in infrared system design," Opt. Eng. **51**(9), 096401-1 (2012).
2. P. Castelein, F. Marion, J.-L. Martin, *et al.*, "Megapixel HgCdTe MWIR focal plane array with a 15-um pitch," in *Detectors and Associated Signal Processing*, vol. 5251 (SPIE, 2004), pp. 65–72.
3. R. L. Strong, M. A. Kinch, and J. M. Armstrong, "Performance of 12-µm- to 15-µm-Pitch MWIR and LWIR HgCdTe FPAs at Elevated Temperatures," J. Electron. Mater. **42**(11), 3103–3107 (2013).
4. O. Gravrand, G. Destefanis, S. Bisotto, *et al.*, "Issues in HgCdTe Research and Expected Progress in Infrared Detector Fabrication," J. Electron. Mater. **42**(11), 3349–3358 (2013).
5. L. Shkedy, E. Armon, E. Avnon, *et al.*, "HOT MWIR detector with 5 um pitch," in *Infrared Technology and Applications XLVII*, vol. 11741 (SPIE, 2021), pp. 146–157.
6. O. Gravrand, C. Lobre, J. L. Santailler, *et al.*, "Design of a small pitch (7.5 μm) mwir hgcdte array operating at high temperature (130k) with high imaging performances," in *Infrared Technology and Applications XLVIII*, vol. 12107 (SPIE, 2022), pp. 207–214.
7. E. Huang, J. Thomas, D. Hibberd, *et al.*, "Small pixel MWIR sensors for low SWaP applications," in *Infrared Technology and Applications XLVII*, vol. 11741 (SPIE, 2021), pp. 123–129.
8. T. Hardy, M. Baril, J. Pazder, *et al.*, "Intra-pixel response of infrared detector arrays for jwst," in *High Energy, Optical, and Infrared Detectors for Astronomy III*, vol. 7021 (SPIE, 2008), pp. 711–722.
9. S. T. Bryson, P. Tenenbaum, J. M. Jenkins, *et al.*, "The kepler pixel response function," The Astrophys. J. Lett. **713**(2), L97–L102 (2010).
10. T. Hardy, C. Willot, and J. Pazder, "Intra-pixel response of the new jwst infrared detector arrays," in *High Energy, Optical, and Infrared Detectors for Astronomy VI*, vol. 9154 (SPIE, 2014), pp. 750–761.
11. P.-E. Crouzet, L. Duvet, P. Strada, *et al.*, "Comparison of persistence in spot versus flat field illumination and single pixel response on a euclid hawaii-2rg at estec," in *High Energy, Optical, and Infrared Detectors for Astronomy VII*, vol. 9915 (SPIE, 2016), pp. 484–497.
12. S. Bustillos Vasco, N. Baier, C. Lobre, *et al.*, "Modulation transfer function measurements by electron-beam-induced current of hgcdte planar diode with small pitch and high operating temperature," Journal of Electronic Materials pp. 1–8 (2023).
13. G. Boreman and E. Dereniak, "Method for measuring modulation transfer function of charge-coupled devices using laser speckle," Opt. Eng. **25**(1), 250148 (1986).
14. K. J. Barnard, I. Anisimov, and J. E. Scheihing, "Random laser speckle based modulation transfer function measurement of midwave infrared focal plane arrays," Opt. Eng. **51**(8), 083601 (2012). Publisher: SPIE.
15. K. J. Barnard, E. L. Jacobs, and P. J. Plummer, "Accuracy and uncertainty in random speckle modulation transfer function measurement of infrared focal plane arrays," Opt. Eng. **55**(12), 121729 (2016). Publisher: SPIE.
16. P. J. Plummer, K. J. Barnard, and M. A. Marciniak, "Investigation of speckle imagery spectral estimation challenges for modulation transfer function measurements," Opt. Eng. **58**(07), 077106 (2019).
17. P. J. Plummer, K. J. Barnard, and M. A. Marciniak, "Generalized focal plane array modulation transfer function estimation approach for nonstationary laser speckle random processes," Opt. Eng. **61**(06), 064104 (2022).
18. I. Shtrichman, T. Fishman, U. Mizrahi, *et al.*, "Spatial resolution of SCD's InSb 2D detector arrays," (Orlando, Florida, USA, 2007), p. 65423M.
19. O. Gravrand, J. Desplanches, C. Delbegue, *et al.*, "Study of the spatial response of reduced pitch hg 1- x cd x te dual-band detector arrays," J. Electron. Mater. **35**(6), 1159–1165 (2006).
20. L. Martineau, L. Rubaldo, F. Chabuel, *et al.*, "Mtf optimization of mct detectors," in *Sensors, Systems, and Next-Generation Satellites XVII*, vol. 8889 (SPIE, 2013), pp. 309–318.
21. J. Berthoz, L. Rubaldo, M. Maillard, *et al.*, "Mtf performance: measurements, modelisation, and optimization for sofradir ii-vi ir photodetectors," in *Quantum Sensing and Nanophotonic Devices XII*, vol. 9370 (SPIE, 2015), pp. 122–132.
22. L. Zhong, X. Li, M. Zhu, *et al.*, "Improved intra-pixel sensitivity characterization based on diffusion and coupling model for infrared focal plane array photodetector," Sensors **21**(24), 8195 (2021).
23. A. Bergeron, M. Terroux, L. Marchese, *et al.*, "Diffraction limit investigation with sub-wavelength pixels," in *Micro- and Nanotechnology Sensors, Systems, and Applications V*, vol. 8725 (SPIE, 2013), pp. 428–436.
24. M. Born and E. Wolff, *Principles of Optics* (Permagon, 1959), pp. 413–419.
25. J. W. Goodman, *Introduction to Fourier optics* (Roberts and Company publishers, 2005), pp. 32–35.
26. B. Liu, K. Liu, M. Zheng, *et al.*, "Vector simulation of pinhole diffraction behavior for high numerical aperture converging incident beam at deep ultraviolet wavelength," in *7th International Symposium on Advanced Optical*

Optics EXPRESS

Manufacturing and Testing Technologies: Design, Manufacturing, and Testing of Micro-and Nano-Optical Devices and Systems, vol. 9283 (SPIE, 2014), pp. 77–84.
27. J.-S. Lee, H.-S. Yang, and J.-W. Hahn, "Wavefront error measurement of high-numerical-aperture optics with a shack-hartmann sensor and a point source," Appl. Opt. **46**(9), 1411–1415 (2007).
28. R. L. Lucke, "Rayleigh-sommerfeld fraunhofer diffraction," arXiv, arXiv:physics/0604229 (2006).
29. J. Primot and N. Guérineau, "Extended Hartmann test based on the pseudoguiding property of a Hartmann mask completed by a phase chessboard," Appl. Opt. **39**(31), 5715–5720 (2000). Publisher: Optica Publishing Group.
30. S. Velghe, J. Primot, N. Guerineau, *et al.*, "Accurate and highly resolving quadri-wave lateral shearing interferometer, from visible to IR," Proc. SPIE - The Int. Soc. for Opt. Eng. **5776**, 134 (2005).
31. S. Velghe, J. Primot, N. Guerineau, *et al.*, "Advanced wave-front sensing by quadri-wave lateral shearing interferometry - art. no. 62920E," (2006), pp. 62920E–1.
32. S. Velghe, J. Primot, N. Guérineau, *et al.*, "Wave-front reconstruction from multidirectional phase derivatives generated by multilateral shearing interferometers," Opt. Lett. **30**(3), 245 (2005).
33. J. Rizzi, "Imagerie de phase quantitative par interférométrie à décalage quadri-latéral. Application au domaine des rayons x durs," phdthesis, Université Paris Sud - Paris XI (2013).
34. V. Lakshminarayanan and A. Fleck, "Zernike polynomials: A guide," J. Mod. Opt. **58**(18), 1678 (2011).
35. A. Stolidi, G. Giakoumakis, J. Primot, *et al.*, "Confidence map tool for gradient-based x-ray phase contrast imaging," Opt. Express **30**(3), 4302–4311 (2022).
36. W. H. Southwell, "Wave-front estimation from wave-front slope measurements," J. Opt. Soc. Am. **70**(8), 998–1006 (1980). Publisher: Optica Publishing Group.
37. K. R. Freischlad and C. L. Koliopoulos, "Modal estimation of a wave front from difference measurements using the discrete Fourier transform," J. Opt. Soc. Am. A **3**(11), 1852–1861 (1986). Publisher: Optica Publishing Group.